



OPEN Single layer dual wideband linear to circular polarisation converter with integrated parasitic elements

Cho Hilary Scott Nkimbeng¹, Heesu Wang¹, Daeyeong Yoon^{1,2}, Yong Bae Park^{1,2}✉ & Ikmo Park¹✉

This paper presents a novel single-layer, single-sided, dual-wideband linear-to-circular (LTC) polarisation converter. The unit cell of the polarisation converter comprises two identical diagonally oriented C-shaped metallic strips arranged symmetrically and integrated with four outwardly extending diagonal parasitic strips. The LTC polarisation converter is placed on the top side of an ultra-thin substrate layer with a profile size of $0.020 \lambda_0$ at 11.9 GHz and $0.05 \lambda_0$ at 30.7 GHz. The inclusion of parasitic strips in the unit cell design is pivotal, inducing a 90° phase shift between the orthogonal wave components, thus enhancing LTC polarisation conversion. The design achieved near-equal transmission amplitudes and maintained a stable phase difference of nearly 90° across two distinct frequency bands, enabling right-hand circular polarisation in the lower frequency band and left-hand circular polarisation in the higher frequency band. Numerical and experimental results showed that the polariser can realise a wideband LTC polarisation conversion for both x- and y-polarised electromagnetic wave incidences at two distinct frequency bands of 6.78–17.08 GHz (fractional bandwidth of 86.3%) and 25.09–36.40 GHz (36.8%). The converter maintained consistent polarisation conversion performance across a broad range of incidence angles and exhibited high and uniform total transmittance in both operational frequency bands.

Keywords Circular polarisation, Linear polarisation, Linear-to-circular polarisation converter, Transmission coefficient, Ultra-wideband

Recently, satellite communication has attracted significant interest in wireless applications^{1,2}. The need for higher data-transmission efficiency and bandwidth optimisation has led to the exploration of advanced technological solutions. Manipulating the polarisation state of electromagnetic waves is a critical aspect of wave propagation in enhancing signal clarity and reducing interference^{3,4}. Metasurfaces are a novel approach adopted in recent years for polarisation manipulation. These engineered materials allow precise control over the amplitude and phase of both reflected and transmitted waves, paving the way for the successful development of numerous metasurface-based polarisation converters. These converters^{5–32} can perform linear-to-circular (LTC) polarisation conversion for linearly polarised (LP) incident electromagnetic waves. LTC polarisation converters operating in transmissive mode have been widely adopted across wireless communication systems because of their broad range of applications and can be designed for single band^{15–27} or dual band, based on the intended application. Single-band LTC polarisation converters are specialised for specific frequency bands, making them ideal for applications in which communication or sensing requirements are confined to a precise frequency range. They provide highly efficient polarisation conversion and maximise performance within their designated band. Dual-band LTC polarisation converters are engineered to operate across two distinct frequency bands, offering greater flexibility and utility for systems operating over a broader spectrum. This dual-band capability is important in scenarios where the equipment must handle multiple communication channels or when spectral efficiency is a priority, such as satellite communications that utilise both the Ku (12–18 GHz) and Ka (26.5–40 GHz) bands.

Several studies have been conducted on dual-band LTC^{28,30–38} polarisation converters. In³⁰, the authors proposed a dual-band transmission-type LTC polarisation converter featuring a periodic array of split-ring resonators and rectangular patches with microstrip rings. This design achieved frequency bands of 6.4–8.8 GHz and 12.1–13.9 GHz with an insertion loss below 1.5 dB. However, the several substrate layers result in bulky structures, and the bandwidths in both frequency bands are narrow. In³¹, the authors proposed a transparent

¹Department of Electrical and Computer Engineering, Ajou University, Suwon 16499, Republic of Korea.

²Department of AI Convergence Network, Ajou University, Suwon 16499, Republic of Korea. ✉email: yong@ajou.ac.kr; ipark@ajou.ac.kr

dual-band LTC polarisation converter using bi-layered chiral metamaterial with an inverted “G” array for the two distinct frequency bands of 8.6–10.9 GHz and 18.1–22.5 GHz. Although they achieved right-hand circular polarisation (RHCP) and left-hand circular polarisation (LHCP) in both bands using a single substrate layer, the bandwidths were narrow for both bands. In³², a split circular ring resonator enclosed in a square ring was employed, and three square patches were added to achieve LP-to-CP conversion in two distinct bands. The operational bandwidths were 11.05–16.75 GHz and 34.16–43.03 GHz. The single-layer substrate significantly reduced the structural profile. However, the achieved bandwidths were narrow for both frequency bands. In³³, a dual-band LTC polarisation converter based on a single-layer dielectric substrate was proposed. The converter element comprised two identical metallic layers, each consisting of a combination of a connected Jerusalem cross and an “I”-type dipole. The proposed design was operational within the frequency ranges of 17.7–20.2 GHz and 27–30 GHz, targeting K-/Ka-band satellite communications. However, the bandwidths achieved for these bands were relatively narrow. In²⁸, a novel dual-circularly polarised transmission (DCT) metasurface was presented. The DCT metasurface comprised a thin substrate with two metal patches arranged in the shape of symmetrical arrows positioned above and below the substrate, achieving LHCP and RHCP waves over the frequency ranges of 7.31–10.58 GHz and 14.26–17.36 GHz, respectively. These bandwidths were relatively narrow for both frequency bands. In³⁴, a dual-band LTC polarisation converter in transmission mode was presented, featuring a unit cell with a square ring enclosing a diagonally split circular ring on a single-layer substrate. LTC polarisation conversion was achieved across two bands: 15.25–19.5 GHz and 33.1–39.9 GHz. However, the bandwidths were relatively narrow for both frequency bands. In³⁵, the authors presented a dual-band LTC planar polarisation converter with six substrate layers separated by foam spacers. The top three layers contained ‘I’-type strips, and the bottom three layers featured Jerusalem crosses. This design achieved frequency bands of 19.4–21.8 GHz and 27.9–30.5 GHz. Despite its dual functionality, the multiple layers made the converter bulky and complex, and the achieved bandwidths were narrow. In³⁶, the authors presented a single-layer dual-band LTC polarisation converter consisting of nonresonant meander lines and strips printed on both sides of a substrate. This design achieved 17.2–21.4 GHz and 27.5–31.2 GHz frequency bands. Although it achieved a low profile, the bandwidths were narrow. In³⁷, the authors proposed a dual-band angular-stable transmissive LP to CP converter based on a metasurface. The design consists of three layers: the top and bottom formed by double split-ring arrays and the central layer containing a square loop nesting a slant dipole. The converter operates over the frequency ranges of 8.77–10.58 GHz and 17.59–19.88 GHz. It achieved a low profile, but the AR bandwidth at both bands was quite narrow. In³⁸, authors presented an ultrathin single-layer transmissive dual-band linear-to-circular polarisation converter. The design consists of dual circular split rings and a connected cross-grid dipole on a Taconic TLY-5 substrate. The converter operates over the frequency ranges of 7.6–9.5 GHz and 18.6–20.9 GHz. Despite the compact size, the AR bandwidth at both frequency bands is narrow. The aforementioned dual-band transmissive LTC polarisation converter metasurfaces^{28,30–38} make it challenging to achieve low-profile wideband operations in both frequency bands.

This study presents a novel structure consisting of two diagonally oriented C-shaped strips incorporating parasitic strips to achieve LTC polarisation in two distinct frequency bands with a single layer. Ultra-wideband LTC polarisation conversion was realised for both x- and y-polarised incident electromagnetic waves in the lower frequency band ranging from 6.78 to 17.08 GHz (fractional bandwidth of 86.3%). A wide LTC polarisation was achieved in the higher frequency band ranging from 25.09 to 36.40 GHz (36.8%). A single-layer substrate was used to achieve an ultra-thin profile size of $0.02 \lambda_0$ and $0.05 \lambda_0$ at the lower and higher frequency bands, respectively, where λ_0 is the free space wavelength at the center frequency of each AR bandwidth (11.9 and 30.7 GHz). In addition, equal transmittances of less than 2.3 dB were achieved in the lower- and higher-frequency bands.

Numerical analysis

To numerically explore the LTC polarisation conversion performance of the proposed design, we conducted a series of simulations using the Ansys high-frequency structure simulator (HFSS) based on the optimised design parameters detailed in the metasurface design. Floquet ports and master-slave boundary conditions facilitated the simulations of the unit cell structure. In these simulations, the unit cell was operated under an incident plane electric field vector oriented at 45° to the x-axis, implying that the magnitude and phase for the electric field components along the x- and y-axis are equal. When an x-polarised wave is incident in the +z direction, it generates a cross-polarisation component (from x to y) characterised by magnitude t_{yx} and phase ϕ_{yx} , in addition to a co-polarisation component (x to x) denoted by t_{xx} . The LTC polarisation conversion is considered successful if it meets two criteria: a phase difference of $\Delta\phi_{yx} = \arg(t_{xx}) - \arg(t_{yx}) = \pm 90^\circ$ and equal amplitudes $|t_{xx}| = |t_{yx}|$.

To accurately determine the effective bandwidth of the ultrawideband LTC polarisation converter, the AR of the transmitted wave was calculated using the equation specified in²⁹. The AR was determined using the transmission coefficients t_{xx} and t_{yx} , along with the phase difference $\Delta\phi_{yx}$. In Fig. 5b, the magnitudes of the transmission coefficients t_{xx} and t_{yx} are within 3 dB difference across the two frequency bands, 6.45–16.72 GHz and 25.06–36.35 GHz. The phase difference $\Delta\phi_{yx}$, which approximates 90° within these specified frequency bands, is shown in Fig. 5a. The AR obtained for the proposed structure remains below 3 dB throughout these dual-frequency bands, as depicted in Fig. 5d, thereby verifying the effectiveness of LTC polarisation conversion. The transmitted wave contains both RHCP and LHCP components. The X-to-CP transmission coefficients were computed using the equations in²⁹.

The magnitude of the X-to-CP transmission coefficient allows identification of the transmitted wave as RHCP or LHCP. In Fig. 1a, the RHCP_{-x} transmission coefficient magnitude exceeds that of LHCP_{-x} within the 6.45–16.72 GHz frequency band. Conversely, the LHCP_{-x} magnitude surpasses the RHCP_{-x} magnitude in the 25.06–36.35 GHz frequency band, indicating that the transmitted wave is RHCP in the 6.45–16.72 GHz band and LHCP in the 25.06–36.35 GHz band. Figure 1b shows the total transmittance computed using the formula

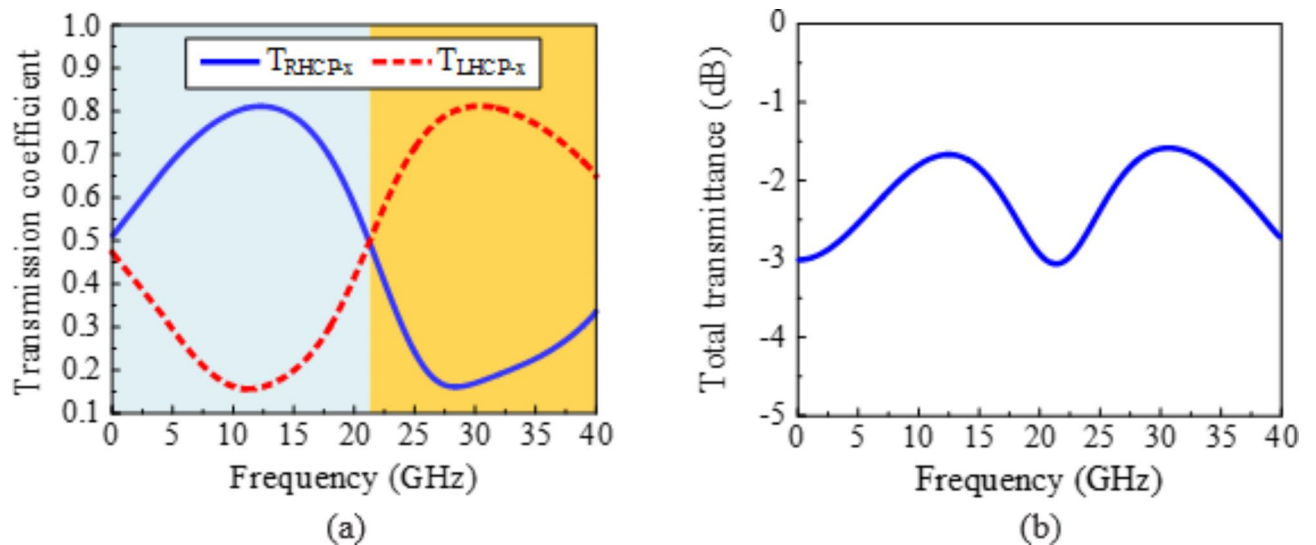


Fig. 1. X-to-CP transmission characteristics of the proposed polarisation converter at X-polarised normal incidence: (a) transmission coefficient and (b) total transmittance.

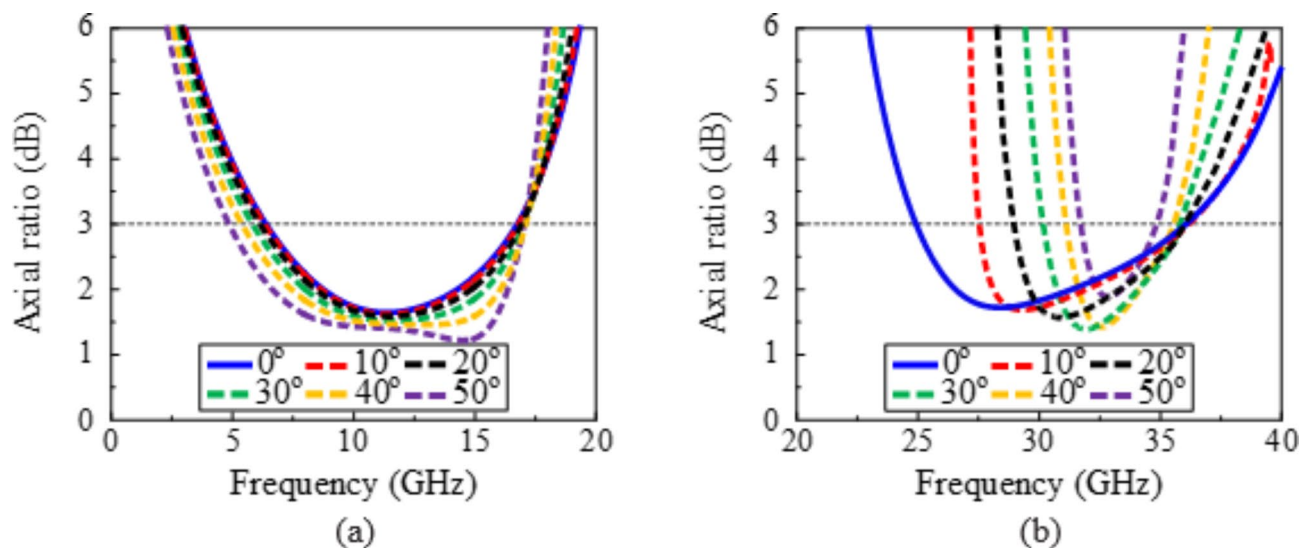


Fig. 2. Simulated axial ratio with respect to the incident angle: (a) lower band and (b) upper band.

$T_{att} = |\Gamma_{ss}|^2 + |\Gamma_{ts}|^2$. The insertion loss of the polarisation converter was kept lower than 2.3 dB within the AR lower frequency band of 6.45–16.72 GHz and higher frequency band of 25.06–36.35 GHz.

Angular stability refers to the ability of the polarisation converter to maintain its performance, particularly the AR when the angle of incidence of the incoming electromagnetic wave is varied. This is an important factor in evaluating the real-life performance of the LTC polarisation converter. To calculate angular stability, we conducted simulations where the angle of incidence was varied at different oblique angles. We evaluated the AR across the operating frequency bands at each angle to assess how well the polarisation conversion performance holds up under non-normal incidence. As shown in Fig. 2a, b, the AR remained above 80% in the lower band and above 20% in the upper band for incident angles less than $\pm 50^\circ$ and $\pm 20^\circ$ for the lower and higher bands, respectively.

Metasurface design

Figure 3 shows the unit cell of the proposed dual-band LTC polarisation converter metasurface, realised in a single layer of a single-sided AD250C substrate. The substrate dimensions for the unit cell are 4.5 mm \times 4.5 mm \times 0.508 mm ($0.18 \lambda_0 \times 0.18 \lambda_0 \times 0.02 \lambda_0$ at 11.9 GHz and $0.46 \lambda_0 \times 0.46 \lambda_0 \times 0.05 \lambda_0$ at 30.7 GHz), with a relative permittivity (ϵ_r) of 2.5 and a loss tangent ($\tan \delta$) of 0.0009. The unit cell comprises two identical diagonally oriented C-shaped metallic strips arranged symmetrically and integrated with four outwardly extending diagonal

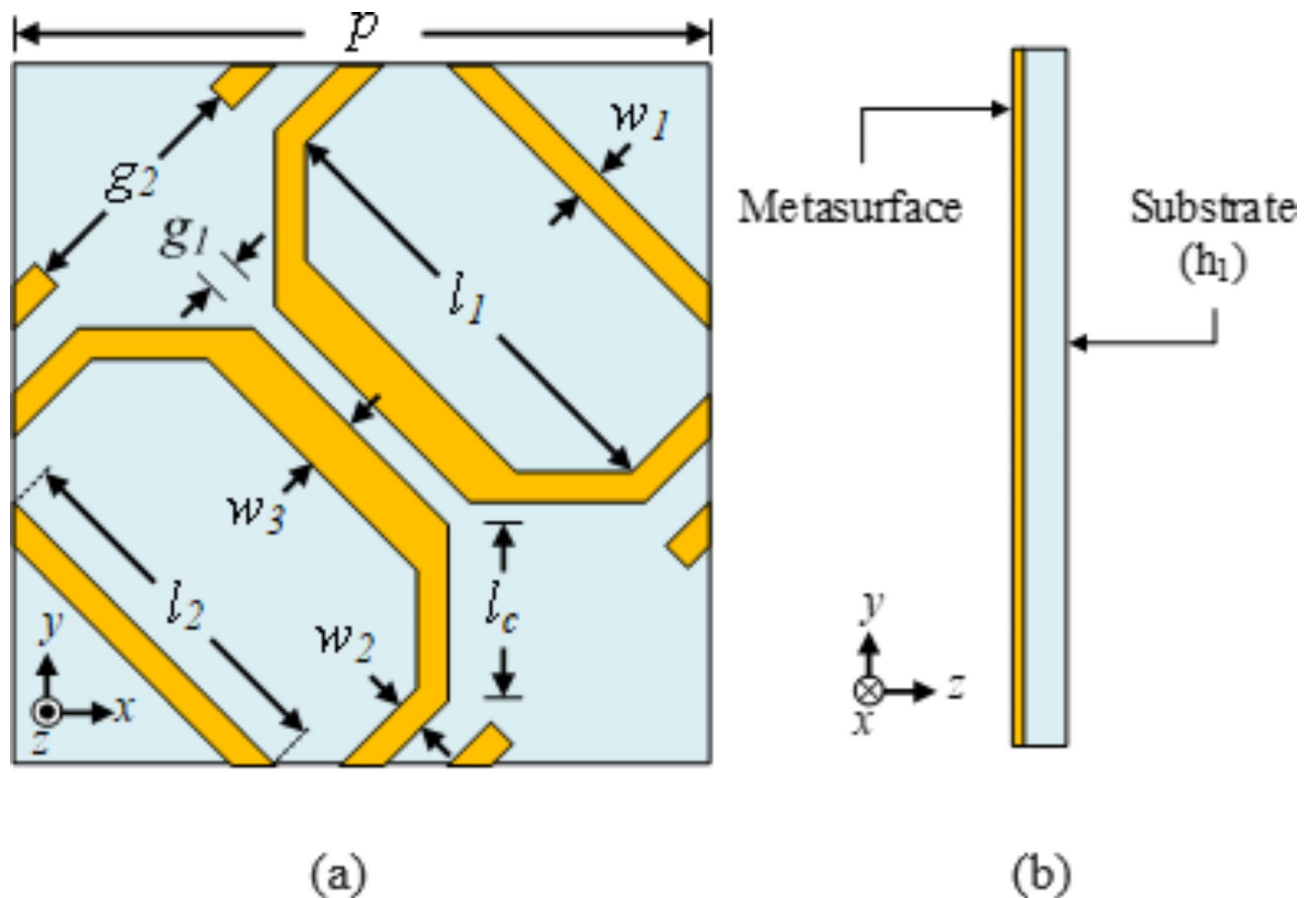


Fig. 3. Unit cell for the proposed structure: (a) top view and (b) side view.

parasitic strips. The entire metallic structure is placed exclusively on the top side of the substrate. The optimised geometrical parameters for the ultra-thin single-layer dual-band LTC polarisation converter were selected as $P = 4.5$ mm, $l_1 = 3$ mm, $l_2 = 2.4$ mm, $w_1 = w_2 = 0.2$ mm, $w_3 = 0.35$ mm, $g_1 = 0.2$ mm, and $g_2 = 1.6$ mm. The design guidelines for the proposed unit cell are as follows:

- A unit cell with two C-shaped metallic elements is positioned diagonally within the cell and arranged symmetrically. The diagonal positioning of the C-shaped elements is instrumental in controlling the polarisation state of the incident electromagnetic waves and a fundamental aspect of the design for dual-band operation.
- The integration of four diagonal parasitic elements with two C-shaped metallic elements enhances the design by providing additional degrees of freedom for tuning the electromagnetic response of the unit cell. These elements significantly contribute to the fine-tuning of the phase difference and amplitude of the transmitted waves. Adjusting the electromagnetic interaction between these elements and the primary C-shaped structures allows precise control over the polarisation conversion process.
- The design parameters of the C-shaped elements and the parasitic extensions are carefully adjusted to their optimal values to achieve near-equal amplitudes and a consistent phase difference of approximately 90° across the two operational frequency bands.

Unit cell design evolution

The design evolution of the proposed dual-band polarisation converter is illustrated in Fig. 4a–d for unit cells A, B, C, and the proposed structure, respectively. A comparison of various unit cell characteristics, such as phase difference, transmission coefficient, total transmittance, and axial ratio (AR), is shown in Fig. 5. Unit cell A features a symmetric metallic pattern, forming a cross-shaped structure, as depicted in Fig. 4a. In Fig. 5a, the phase difference for unit cell A approaches 90° only within the frequency range of 10.94–29.28 GHz. In addition, as indicated in Fig. 5b, the difference between co- and cross-polarisation (t_{xx} and t_{yy}) remains within 5 dB for the lower band (4–32 GHz) and exceeds 8 dB for the higher band (32–40 GHz). The total transmittance, which is less than 2.3 dB within the frequency band of 10.94–29.28 GHz, is shown in Fig. 5c. As illustrated in Fig. 5d, the AR is less than 3 dB in the range of 10.94–29.28 GHz and greater than 4.5 dB in the 33–35 GHz band, resulting in the formation of only a single LTC polarisation band. To enhance the LTC polarisation conversion characteristics, the structure was refined to that of unit cell B, which includes two identical, diagonally oriented C-shaped metallic strips arranged symmetrically, as shown in Fig. 4b. The phase difference for unit cell B is close to 90° only in the range of 6.46–16 GHz, as shown in Fig. 5a. In Fig. 5b, the difference between co- and cross-polarisation (t_{xx}

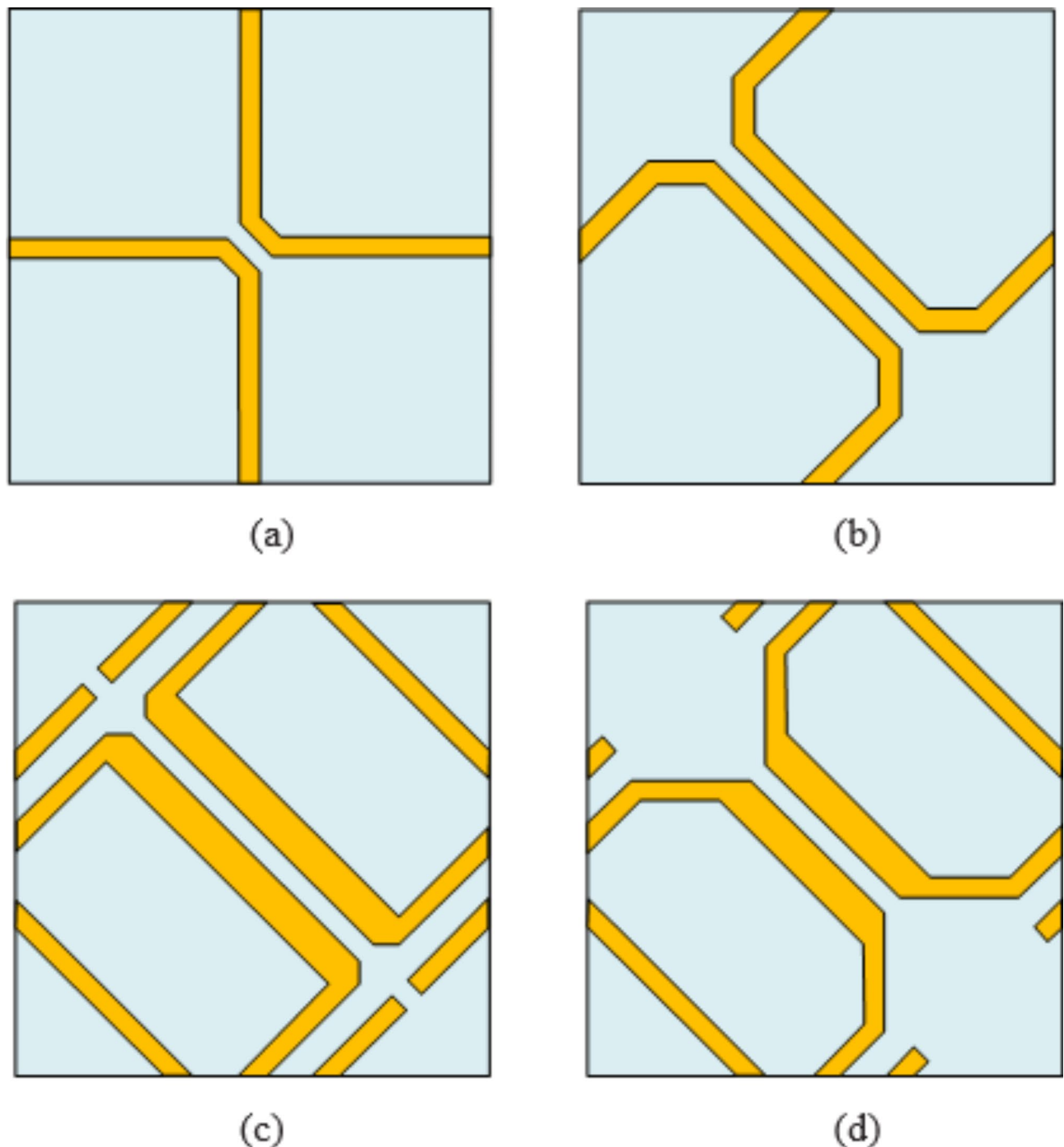


Fig. 4. Unit cell design evolution: (a) unit cell A, (b) unit cell B, (c) unit cell C, and (d) proposed unit cell.

and t_{yx}) for unit cell B remains within 3.5 dB for the lower band (1–20 GHz) and exceeds 9 dB for the higher band (25–40 GHz). The total transmittance is less than 2.2 dB within the frequency band of 6.46–16 GHz, as shown in Fig. 5c. In Fig. 5d, the AR is under 3 dB in the 6.48–16 GHz band and over 4.5 dB in the 28–39 GHz frequency band. To achieve dual-band performance, unit cell B was modified by incorporating parasitic strips to form unit cell C, as shown in Fig. 4c. This design includes two identical diagonally oriented C-shaped metallic strips with four outwardly extending diagonal parasitic strips. These parasitic strips create resonant effects that alter the phase or amplitude of the scattered fields, which can modify the electromagnetic field interactions and improve AR characteristics. As shown in Fig. 5a, the phase difference for unit cell C is approximately 90° in the frequency ranges of 5.4–10 GHz and 18–24 GHz. This characteristic facilitates LTC conversion in these specific frequency bands. In Fig. 5b, the difference between co- and cross-polarisation (t_{xx} and t_{yx}) is maintained within 4 dB for the lower band (4–16 GHz), within 3 dB for the mid-band (19–32 GHz), and within 5 dB for the higher band (33–40 GHz). The total transmittance was within 2.1 dB for the lower frequency bands of 4–10 GHz; however,

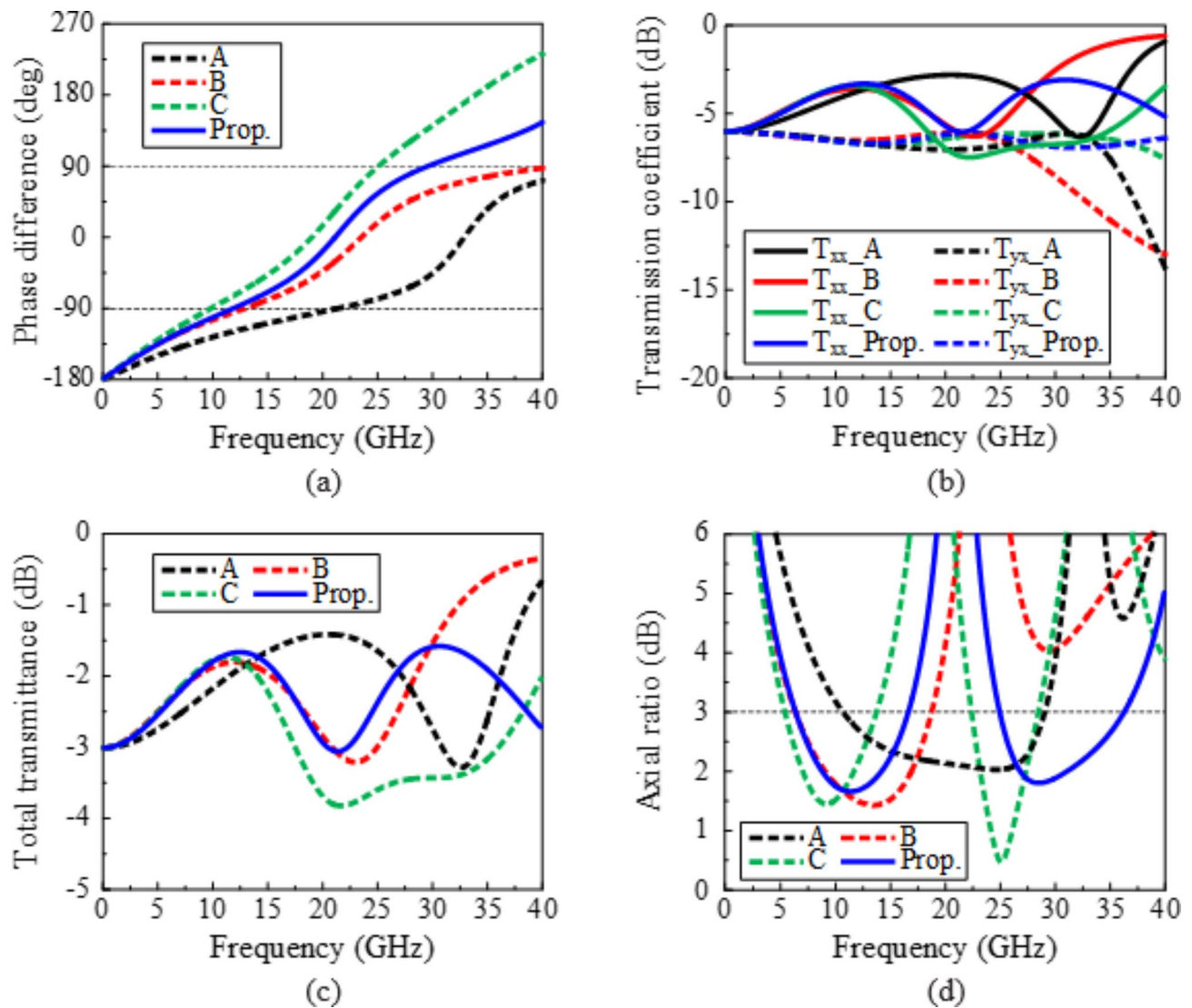


Fig. 5. Comparison of characteristics of various unit cell designs: (a) phase difference, (b) transmission coefficient, (c) total transmittance, and (d) axial ratio.

this is quite low for the frequency bands of 9–32 GHz, as shown in Fig. 5c. A dual-band AR of less than 3 dB was achieved in the lower bands (5.46–10 GHz) and higher bands (18–23 GHz), exceeding 3 dB in the 28–40 GHz band, as demonstrated in Fig. 5d. The AR shifts toward lower frequencies from unit B to unit cell C, primarily due to the introduction of parasitic strips in unit C. These parasitic strips generate additional resonant modes that interact with the electromagnetic field, altering the phase difference and amplitude between the orthogonal wave components. Furthermore, the parasitic strips increase the overall effective electrical length of the unit cell, which results in lower resonant frequencies. This shift in resonance causes the AR bandwidth to move toward lower frequencies. The low transmittance and narrow AR bandwidths for the lower- and higher-frequency bands led to a modification of the design of unit cell C in the proposed structure, as shown in Fig. 4d. The broader widths of the C-shaped strips in unit cell C and the proposed design improve the interaction between the incident electromagnetic waves and the structure, enhancing electromagnetic coupling and transmittance. Additionally, the broader widths help maintain a stable phase difference between the orthogonal components of the incident wave across a wider frequency range, resulting in better AR performance, broader bandwidth, and improved transmission efficiency. In Fig. 5a, the phase difference is approximately 90° in the frequency bands of 6.45–16.72 GHz and 25.06–36 GHz. This proposed design exhibits improved transmission coefficient characteristics in both the lower (4–20 GHz) and higher frequency bands (21–40 GHz), maintaining the difference between co- and cross-polarisation (t_{xx} and t_{yx}) within 5 dB across both bands, as shown in Fig. 5b, compared with the previous designs. A total transmittance of less than 2.3 dB was also achieved in the lower- and higher-frequency bands, as shown in Fig. 5c. Based on the improved phase and transmission characteristics at both the lower and higher frequency bands, wideband LTC was achieved at both bands, with an AR less than 3 dB within the bands of 6.45–16.72 GHz and 25.06–36.35 GHz, as shown in Fig. 5d. Thus, the modified structure with parasitic strips and diagonally oriented C-shaped metallic elements exhibits exceptional dual-band characteristics.

The significant improvement in the AR from unit cell C to the proposed design is primarily due to two key structural modifications: the increased gap between the parasitic elements and the larger corner truncation in the C-shaped strips. These changes improve the phase control and transmission characteristics, directly contributing to improved AR performance. The increased gap between the parasitic elements in the proposed design reduces the electromagnetic coupling between adjacent elements. This wider separation minimizes mutual interference, allowing the elements to resonate more independently. As a result, the phase balance between the orthogonal components of the incident wave becomes more stable. The reduced coupling also ensures that the phase difference between these components remains close to 90° , improving the polarisation conversion and maintaining a lower AR across a broader frequency range. Additionally, the larger corner truncation in the C-shaped strips modifies the current distribution along the strips, altering the resonance characteristics of the design. This adjustment allows for more efficient transmission across a wider frequency range. Optimizing the current path through corner truncation broadens the AR bandwidth, ensuring that the AR stays below 3 dB over a wider range of frequencies, particularly at the higher frequency band.

Current distribution on unit cell

The current distribution was examined to understand the working mechanism of the unit cell. The surface current distribution is plotted for the minimum AR points, 12 and 28 GHz, in Figs. 6 and 7, respectively. At the lower frequency of 12 GHz, high current intensities are observed at the C-strips on the unit cell at 0° , 90° , 180° and 270° , indicating that the inner C-strips are mainly responsible for the AR at the lower frequencies, as shown in Fig. 6. Similarly, as shown in Fig. 7, high currents are observed for both the inner C-strips and parasitic

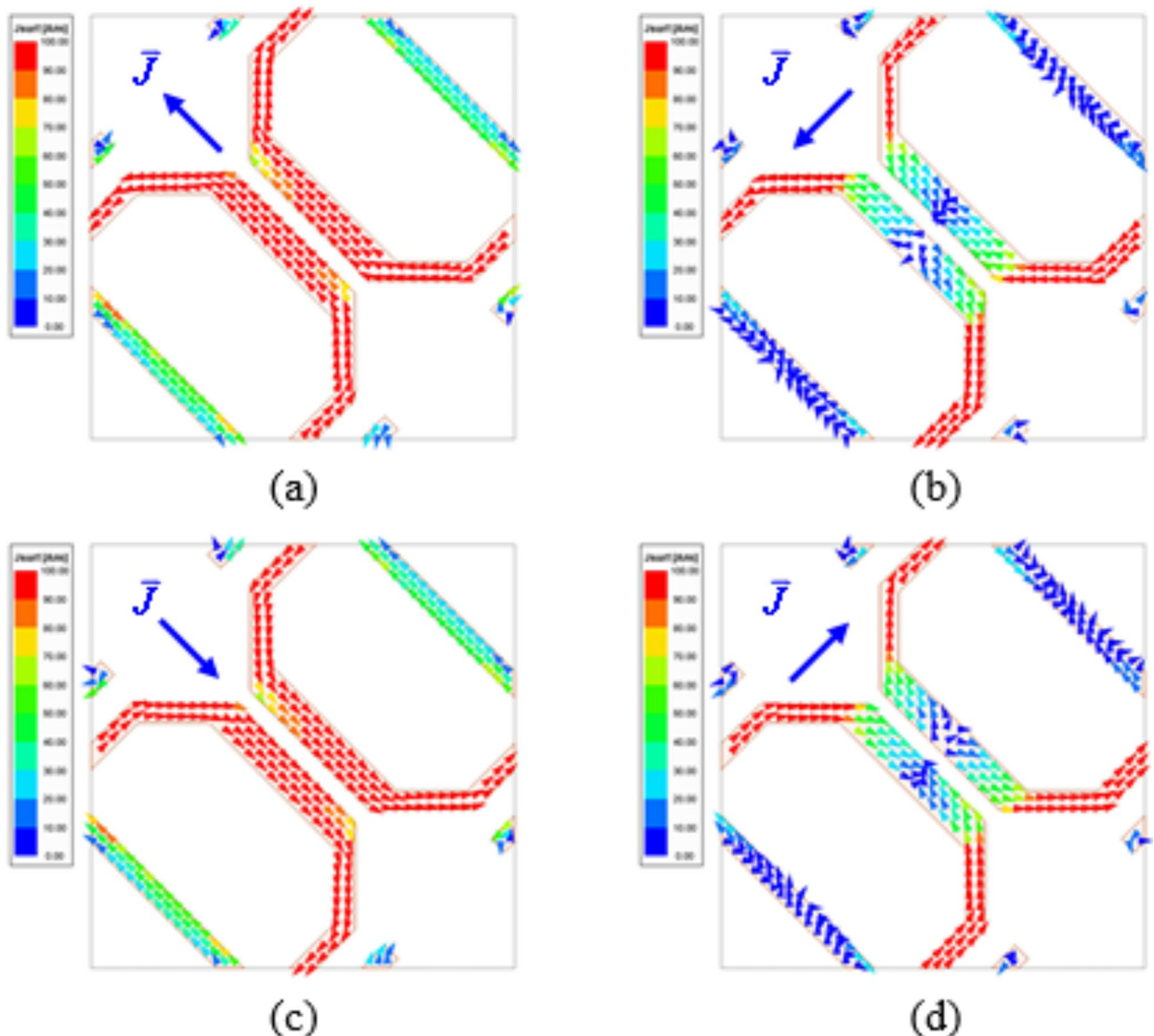


Fig. 6. Surface current density at 12 GHz: (a) $\omega t = 0^\circ$, (b) $\omega t = 90^\circ$, (c) $\omega t = 180^\circ$, and (d) $\omega t = 270^\circ$.

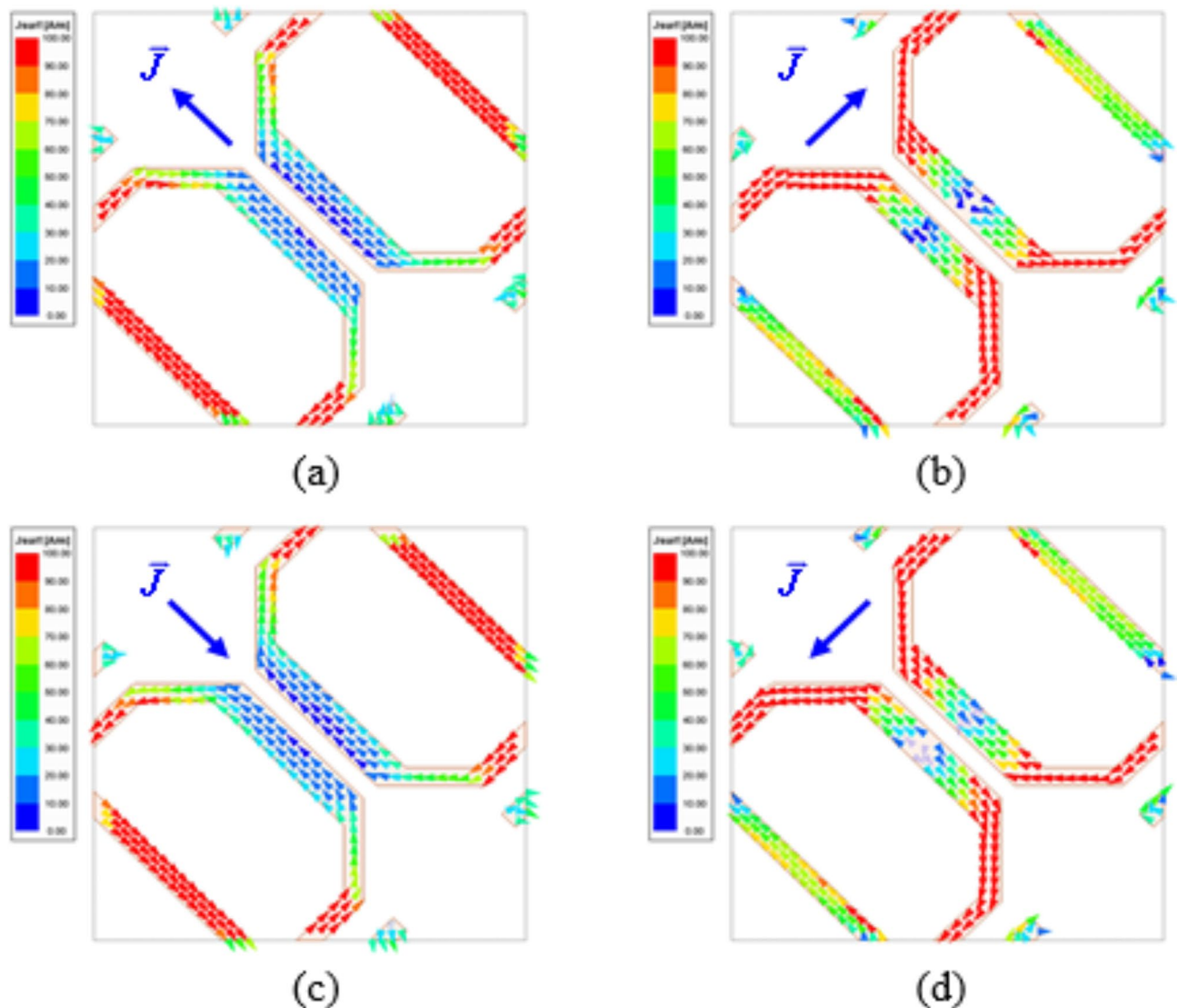


Fig. 7. Surface current density at 28 GHz: (a) $\omega t = 0^\circ$, (b) $\omega t = 90^\circ$, (c) $\omega t = 180^\circ$, and (d) $\omega t = 270^\circ$.

patches at 0° , 90° , 180° , and 270° , indicating that the higher AR frequency band is a result of the interplay between the inner C-strips and outer parasitic patches.

To further elucidate the RHCP in the lower frequency band and LHCP in the higher frequency band, the surface current vectors at different intervals ($\omega t = 0^\circ$, $\omega t = 90^\circ$, $\omega t = 180^\circ$, $\omega t = 270^\circ$) were examined at the AR minimum points, specifically at 12 GHz for the lower and 28 GHz for the higher frequency bands, as shown in Figs. 6 and 7, respectively. In Fig. 6a, at $\omega t = 0^\circ$, in the lower frequency band (12 GHz), the initial orientation of the surface current vectors is predominantly upwards, suggesting alignment along the positive y-axis. This orientation serves as the starting point for the RHCP cycle. Progressing to $\omega t = 90^\circ$, in Fig. 6b, the vectors display a 90° counterclockwise rotation from their initial orientation, now lying horizontally downwards along the negative y-axis. This quarter-period phase advancement is a characteristic of RHCP. Continuing to $\omega t = 180^\circ$, the vectors have undergone another 90° rotation as expected, aligning downwards along the negative y-axis, as depicted in Fig. 6c. Finally, at $\omega t = 270^\circ$, the vectors complete a 270° cumulative rotation, pointing horizontally to the right (positive x-axis), as shown in Fig. 6d. This demonstrates a three-quarter period phase progression consistent with the counterclockwise rotation of the RHCP in the lower frequency band.

Similarly, the surface currents at different intervals ($\omega t = 0^\circ$, 90° , 180° , and 270°) were also examined at 28 GHz to demonstrate the formation of LHCP. Sequential clockwise rotation of the surface current vectors is indicative of LHCP. As shown in Fig. 7a, at $\omega t = 0^\circ$, the surface current vectors are oriented upwards. This initial state signifies the beginning of the LHCP cycle. Moving to $\omega t = 90^\circ$, there is a notable 90° clockwise rotation, with the current vectors now pointing to the right, as shown in Fig. 7b. This transition coincides with the first-quarter phase shift, which is essential for generating LHCP. At $\omega t = 180^\circ$, the vectors continue this clockwise pattern, which positions them downwards, thus confirming a half-period phase shift as depicted in Fig. 7c. Finally, at $\omega t = 270^\circ$, the vectors are expected to have completed a 270° cumulative clockwise rotation, pointing to the

left, as shown in Fig. 7d. This represents a three-quarter-period phase shift, maintaining a consistent clockwise rotation associated with LHCP in the higher-frequency band.

The polarisation conversion mechanism is driven by the interaction between the diagonally oriented C-shaped metallic strips and the parasitic strips. The C-shaped strips induce a 90° phase shift between the orthogonal components of the incident wave due to their specific geometrical configuration and resonance properties. This phase shift is crucial for achieving CP because it creates the necessary phase delay between the orthogonal electric field components of the incident wave. The surface currents primarily resonate along the C-shaped elements at the lower frequency range. This resonance occurs because the dimensions of the C-shaped strips correspond closely to the wavelength of the incident wave at these frequencies, leading to efficient coupling and strong current flow along the strips. The result is the induction of a 90° phase shift between the orthogonal components of the electric field, which produces RHCP. As the frequency increases, the electrical size of the C-shaped elements becomes smaller relative to the wavelength, and the parasitic strips come into play. These parasitic strips introduce additional resonant modes that modify the electromagnetic field's phase response. The interaction between the C-shaped elements and parasitic strips at these higher frequencies creates a reversed 90° phase shift, resulting in LHCP. This dual-band behavior was confirmed through surface current distribution analysis, where distinct current rotations were observed at different frequency bands. Specifically, at 12 GHz, the surface currents rotated counterclockwise, indicating RHCP, while at 28 GHz, the surface currents rotated clockwise, confirming LHCP, as shown in Figs. 6 and 7, respectively. This demonstrated the structure's ability to convert the incident wave to RHCP in the lower band and LHCP in the higher band.

Parametric study

This study explored the impact of crucial parameters on the characteristics of the unit cell. Simulations were conducted to optimise an ultrathin dual-band unit cell with parasitic strips. Initially, the unit cell response was assessed with all parameters set to their optimal values. Subsequently, a parametric study was conducted, varying the design parameters one at a time. The effect of varying the cut size of the diagonal-oriented C-shaped strip (l_c) on the phase difference, transmittance, and AR is shown in Fig. 8a–c, respectively. In Fig. 8a, as the cut size (l_c) increases from 0.2 to 0.8 mm, the phase difference improves in the lower frequency band and deteriorates in the higher frequency band. An increase in cut size (l_c) leads to improved transmittance in both the lower- and higher-frequency bands, as depicted in Fig. 8b. The AR bandwidth shifts to the lower frequencies as the cut size (l_c) increases from 0.2 mm to 0.8 mm in both the lower and higher frequency bands as shown in Fig. 8c.

The effect of varying the gap size of the two diagonally positioned C-shaped strips (g_1) on the phase difference, transmittance, AR is shown in Fig. 9a–c, respectively. An increase in gap size (g_1) from 0.2 mm to 0.8 mm led to a deterioration of the phase difference at the lower frequency band and an improvement of the phase difference at the higher frequency, as shown in Fig. 9a. Furthermore, in Fig. 9b, increasing the gap size (g_1) enhances the transmittance at lower frequency bands while shifting the transmittance at the higher frequency band upwards. With a gap size of $g_1 = 0.2$ mm, equal transmittance at lower frequencies is achieved despite the reduced transmittance at both lower and higher frequencies. As shown in Fig. 9c, AR improves at lower and higher frequency bands with an increase in gap size (g_1).

The effect of varying the width of the diagonal C-shaped strip (w_3) on the phase difference, transmittance, and AR is shown in Fig. 10a–c, respectively. An increase in the width of the diagonal C-shaped strip (w_3) from 0.35 mm to 0.75 mm leads to an improvement in the phase difference at the lower and higher frequency bands, as shown in Fig. 10a. In Fig. 10b, the electromagnetic transmittance deteriorates in the lower-frequency band, as the width of the diagonal C-shaped strip (w_3) increases and improves in the higher-frequency band. In Fig. 10(c), AR improves in the lower and higher frequency bands as the diagonal C-shaped strip (w_3) increases.

The effects of varying the inner width of the diagonal C-strip (w_2) on the phase difference, transmittance, and AR are shown in Fig. 11a–c, respectively. The inner width of the diagonal C-shaped strip (w_2) has a significant impact on the unit cell's performance, directly influencing the electromagnetic characteristics of the structure because the C-shaped strip is the primary resonating element. Wider strips increase the current path length, which alters the inductive and capacitive properties. This change affects the resonance frequencies, phase

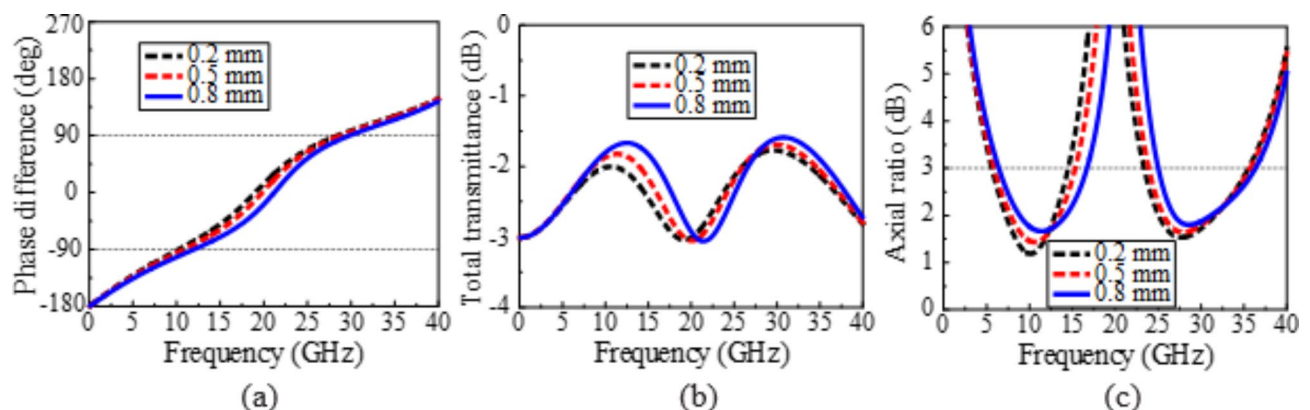


Fig. 8. Effect of cut size of C-shaped diagonal strip (l_c): (a) phase, (b) transmittance, and (c) axial ratio.

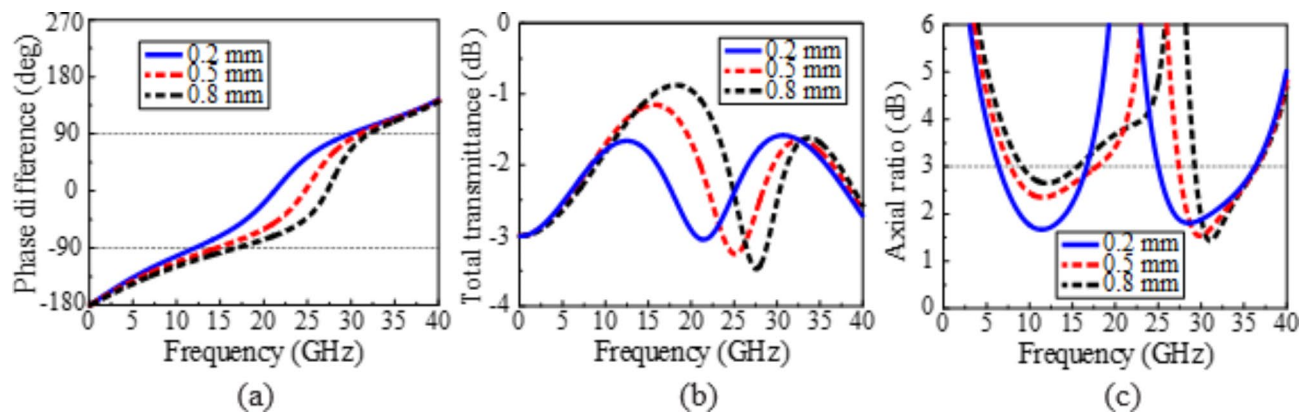


Fig. 9. Effect of gap size (g_1): (a) phase, (b) transmittance, and (c) axial ratio.

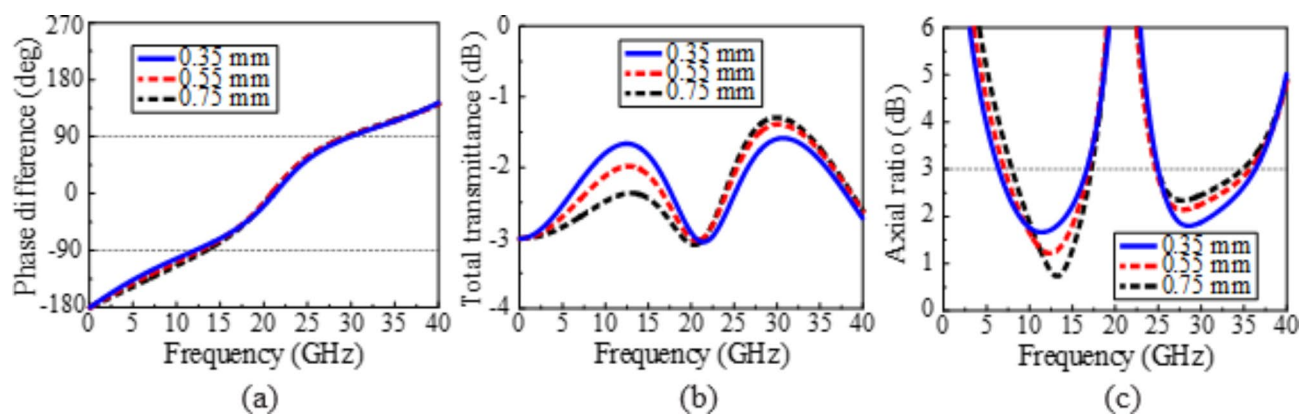


Fig. 10. Effect of width (w_3): (a) phase, (b) transmittance, and (c) axial ratio.

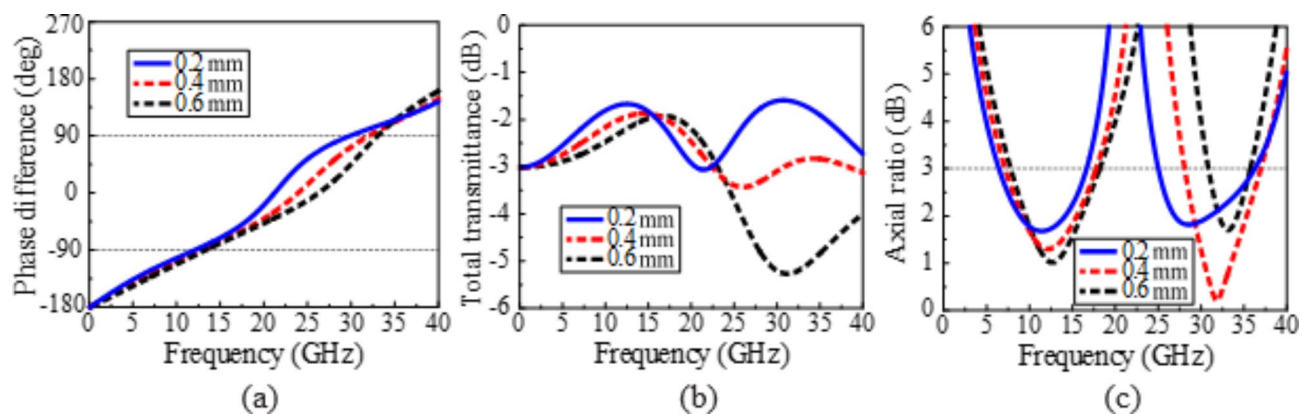


Fig. 11. Effect of width (w_2): (a) phase, (b) transmittance, and (c) axial ratio.

response, and transmission characteristics. An increase in the inner width of the diagonal C-strip (w_2) from 0.2 mm to 0.6 mm primarily causes phase difference deterioration in the higher frequency band, as shown in Fig. 11a. This occurs because widening the C-shaped strip alters the current distribution, increases the electrical path length, and shifts the resonance condition. At higher frequencies, these changes lead to an imbalance in the inductive and capacitive characteristics, resulting in the observed phase deterioration. In Fig. 11b, an increase in the inner width of the diagonal C-strip (w_2) from 0.2 mm to 0.6 mm shows a decrease in electromagnetic transmittance in both the lower and higher frequency bands. This happens because the wider strip reduces the efficiency of electromagnetic wave coupling, leading to higher losses and lower transmission. In addition, AR improves in lower band and deteriorates higher frequency band as the width of the parasitic strip (w_2) increases,

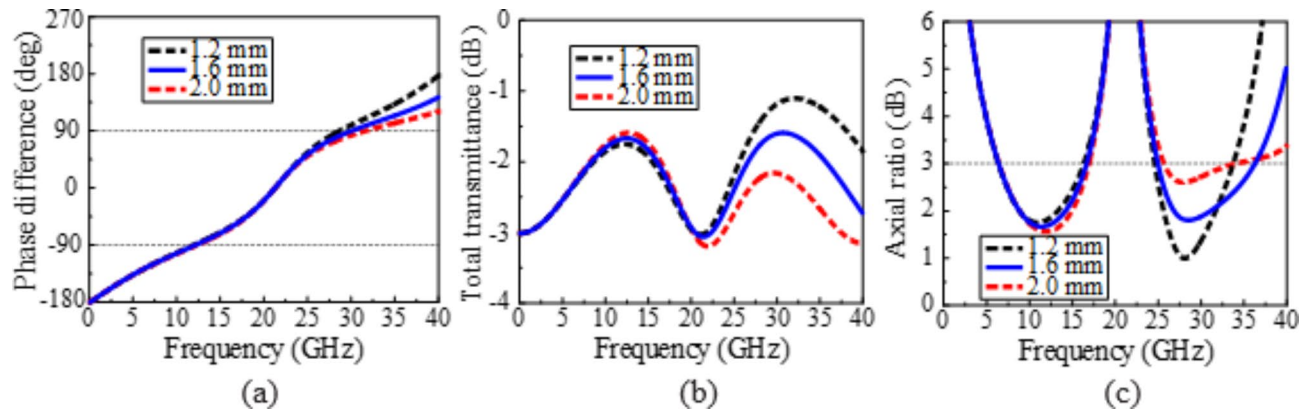


Fig. 12. Effect of gap size (g_2): (a) phase, (b) transmittance, and (c) axial ratio.

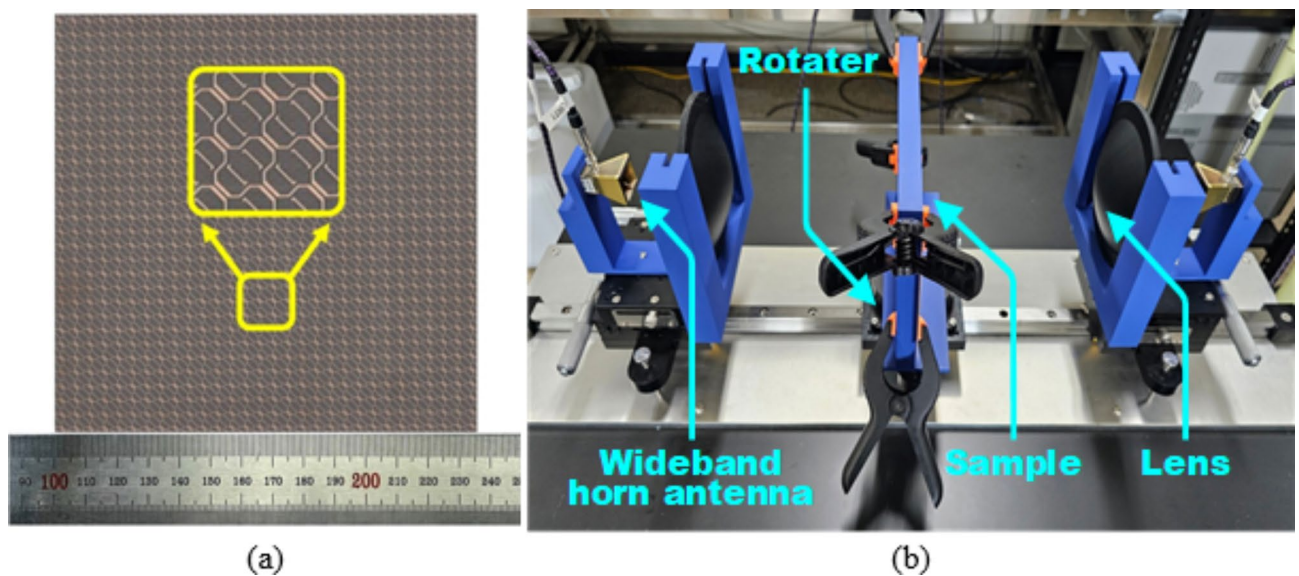


Fig. 13. (a) Fabricated sample and (b) measurement setup.

as shown in Fig. 11c. This degradation in the higher frequency band is due to the disrupted phase balance and reduced transmittance, which affect the structure's ability to maintain circular polarisation at higher frequencies.

The effects of the gap size of the parasitic strip (g_2) on the phase difference, transmittance, and AR are shown in Fig. 12a–c, respectively. An increase in the gap size (g_2) from 1.2 to 2 mm leads to an improvement in the phase difference in the higher frequency band as the phase difference approaches 90°, as shown in Fig. 12a. In Fig. 12b, as gap size increases, transmittance improves in the higher-frequency band and decreases slightly in the lower-frequency band. Furthermore, as the gap size increases, the AR shifts to higher frequencies within the lower frequency band, whereas in the higher frequency band, the AR bandwidth improves as the gap size increases from 1.2 to 1.6 mm. However, a further increase in gap size leads to a deterioration of AR at higher frequencies, as shown in Fig. 12c.

Measurement results

To validate the efficacy of the proposed ultrathin dual-band LTC polarisation conversion structure, a prototype was constructed using conventional printed circuit board fabrication methods. This prototype consisted of 30×30 cells, encompassing a total area of $150 \times 150 \text{ mm}^2$, as depicted in Fig. 13a. The experimental setup, shown in Fig. 13b, features a horn antenna mounted on a rail system that allows adjustable positioning relative to the sample, thereby ensuring optimal distance control. Precision in movement and positioning is achieved using an xyz-position stage that holds the sample at a constant distance equal to the focal length of the horn antenna. The inclusion of a rotating stage on the sample holder facilitates adjustments to the incidence angle, enabling transmittance measurements at varying orientations while keeping the antenna direction fixed. The focusing-lens horn antenna was selected to mitigate the effects of reflection and diffraction, effectively minimising the diffraction typically caused by mounting clamps. This choice ensures that such effects are inconsequential to the

measurement results. The connection between the horn antenna and the vector network analyser (VNA) employs a waveguide-to-coaxial adapter, flange, and cables, creating a stable and precise linkage for data acquisition. As illustrated in Fig. 13b, the measurement configuration employs two horn antennas connected to an Agilent VNA (N5230C) with the prototype strategically positioned between them. This setup allows the emission of vertically polarised (x-polarised) incident waves from one antenna and the reception of the corresponding transmitted waves by the other, enabling the determination of the transmission coefficient t_{xx} . By rotating the receiving horn antenna by 90° and while maintaining the transmitting horn in its position, the transmission coefficient t_{yx} can also be measured. The experimental findings shown in Fig. 14 demonstrate a substantial similarity to those of our simulations. As shown in Fig. 14a, the measured 3 dB AR bandwidth of 6.78–17.08 GHz (86.3%) and 25.09–36.40 GHz (36.8%) both for the lower and higher frequency bands closely align with the simulated ranges of 89.3% and 36.7%, which span 6.45–16.72 GHz and 25.06–36.35 GHz, respectively. Similarly, Fig. 14b indicates that the measured transmittance within the AR bandwidth from -2.12 dB to -1.31 dB and -2.20 dB to -1.48 dB for the lower and higher bands, closely parallels the simulated transmittance range of -2.62 dB to -1.43 dB and -2.29 dB to -1.57 dB for both frequency bands of 6.45–16.72 GHz and 25.06–36.35 GHz, respectively. In addition, as shown in Fig. 14c, the simulated and measured phase differences were approximately 90° in the frequency bands of 6.45–16.72 GHz and 25.06–36.35 GHz. Similarly, as shown in Fig. 14d, the simulated and measured transmission coefficient characteristics in both the lower (6–18 GHz) and higher frequency bands (25–37 GHz) maintained a difference within 5 dB between co- and cross-polarisation (t_{xx} and t_{yx} , respectively) across both bands. The discrepancy between the measured and simulated total transmittance values can be attributed to external factors, such as small reflections or diffraction effects, which were present during the measurement process despite efforts to minimize them using focusing-lens antennas.

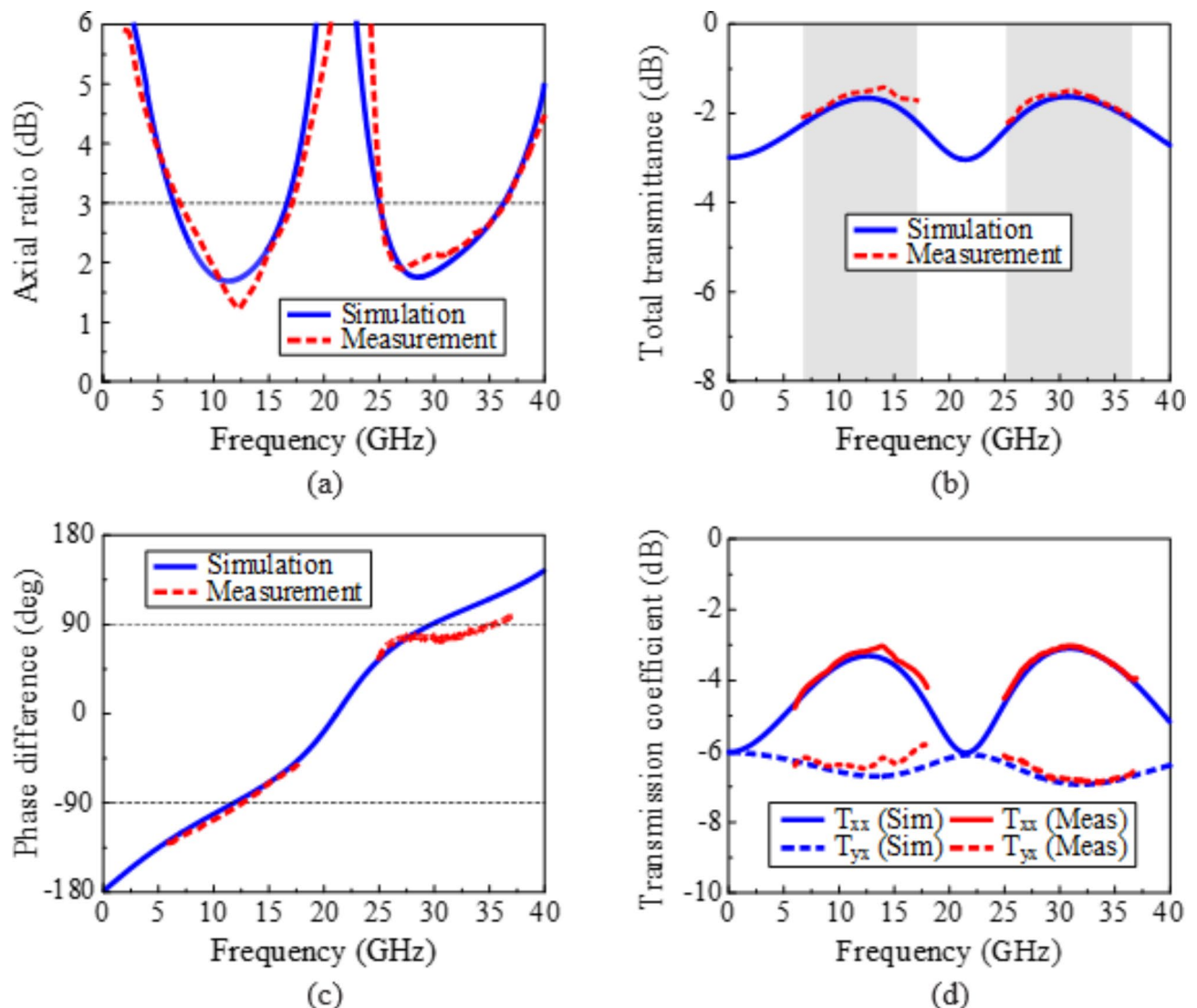


Fig. 14. Measured and simulated results: (a) AR, (b) transmittance, (c) phase, and (d) transmission coefficient.

Comparison

Table 1 presents a detailed performance comparison between the proposed dual-band LTC polarisation converter and other notable dual-band converters reported in the literature^{28,30–38}. The selection criteria for the comparison table included design profile size, AR bandwidth, insertion loss, and angular stability. The converter in³⁰ has a thickness of $0.23 \lambda_0$ in the lower band and $0.39 \lambda_0$ in the higher band, whereas the proposed design reduces this to $0.02 \lambda_0$ and $0.05 \lambda_0$, respectively, making the converter much thinner. In addition, the proposed converter achieved significantly broader AR bandwidths and better angular stability than those in³⁰. The design in³¹ has a thickness of $0.049 \lambda_0$ in the lower frequency band and $0.10 \lambda_0$ in the higher band, which is much thicker than our structure. Additionally, the proposed converter offers broader AR bandwidths than the design in³¹ and better angular stability for both bands. Although the converter in³² has a better profile size of $0.006 \lambda_0$ in the lower frequency band compared to that of the proposed design, it has a thicker profile of $0.016 \lambda_0$ in the higher frequency band compared to our design. The proposed converter offers broader AR bandwidths of 86.8% and 36.8% compared to 41% and 23%. Although the insertion loss in³² is 2.3 dB in the lower band and 2 dB in the higher band, the proposed design maintains the insertion loss of 2.3 dB for both bands. In addition, the proposed design provides slightly better angular stability in the lower band and comparable stability in the higher band. Consequently, the proposed design significantly reduces the profile size compared to the design in³³, with thickness of $0.1 \lambda_0$ and $0.15 \lambda_0$ in the lower and higher frequency bands, respectively. Additionally, the proposed converter achieves broader AR bandwidths compared to the 29% and 12% in³³. Although the converter in³³ has a lower insertion loss of 2 dB in the lower band and 0.8 dB in the higher band, the proposed design offers superior angular stability of 50° in the lower band and 20° in the higher band. The converter design in²⁸ has a thickness of $0.089 \lambda_0$ in the lower frequency band and $0.158 \lambda_0$ in the higher frequency band, which is bulkier than that of the proposed design. The proposed design also achieved significantly broader AR bandwidths compared to the 36.6% and 19.6% in the reference design. In³⁴, a lower profile size of $0.017 \lambda_0$ in the lower band and $0.036 \lambda_0$ in the higher band were achieved compared to the proposed design's $0.02 \lambda_0$ and $0.05 \lambda_0$, respectively. The design in³⁴ had a better insertion loss of 1.6 dB at the lower frequencies than that of the proposed design, 2.3 dB; the insertion loss of the proposed design is better at higher frequencies. The proposed converter achieved broader AR bandwidths compared to the 25% and 16.4% in³⁵, and the proposed design is significantly thinner than the converter in³⁵, which has profile sizes of $0.98 \lambda_0$ in the lower band and $1.39 \lambda_0$ in the higher band. Although the insertion loss in³⁵ is lower at 0.5 dB for the lower band and 0.4 dB for the higher band, the proposed design achieved superior AR bandwidths compared to the narrow AR bandwidths of 11.7% and 8.9% in³⁶. The proposed design has a lower profile than that in³⁶, which has a profile size of $0.097 \lambda_0$ in the lower band and $0.147 \lambda_0$ in the higher band. Even though the insertion loss in³⁶ is lower at 0.5 dB for the lower band and 0.6 dB for the higher band, it achieved narrow AR bandwidths of 21.8% and 12.6%, respectively, compared to the proposed design. Additionally, the proposed design has better angular stability when compared to³⁶. The converter in³⁷ has better angular stability as well as a lower insertion loss of 1.37 dB at the lower frequency compared to the proposed converter. However, its profile sizes of $0.032 \lambda_0$ in the lower band and $0.062 \lambda_0$ in the higher band are thicker than those of the proposed design. Additionally, the bandwidths achieved at both frequency bands (18.7% and 12.2%) were relatively narrow compared to those of the proposed design. The proposed design also achieves better insertion loss at a higher frequency compared to³⁷. The converter in³⁸

Ref. No	T (λ_0)	CS (λ_0)	IL (dB)	BW (%)	AS ($^\circ$)	No of ML	CF (GHz)
30	0.23 0.39	0.22×0.23 0.38×0.40	–	31.6 13.8	25 –	4	7.6 13.0
31	0.049 0.10	0.13×0.13 0.27×0.27	–	23.6 21.7	40 –	2	9.75 20.3
32	0.006 0.016	0.24×0.24 0.66×0.66	2.3 2	41 23	45 30	1	13.9 38.6
33	0.1 0.15	0.25×0.25 0.39×0.39	2 0.8	29 12	20 –	2	18.5 29
28	0.089 0.158	0.30×0.30 0.53×0.53	–	36.6 19.6	–	2	8.9 15.8
34	0.017 0.036	0.30×0.30 0.63×0.63	1.6 2.8	25.1 16.5	–	2	17.3 36.1
35	0.98 1.39	0.49×0.49 0.70×0.70	0.5 0.4	11.7 8.9	–	6	20.6 29.2
36	0.097 0.147	0.17×0.19 0.25×0.29	0.5 0.6	21.8 12.6	45 –	1	19.3 29.35
37	0.032 0.062	0.27×0.27 0.52×0.52	1.37 2.9	18.7 12.2	60 –	2	9.68 18.74
38	0.019 0.039	0.21×0.21 0.42×0.42	2.91 2.96	22.5 11.8	35 –	1	11.3 23.2
Proposed	0.02 0.05	0.18×0.18 0.46×0.46	2.3 2.3	86.8 36.8	50 20	1	11.9 30.7

Table 1. Performance comparison of the existing and proposed dual-band LTC polarisation converters. *T* Thickness, *CS* cell size, *IL* insertion loss, *BW* 3 dB AR bandwidth, *AS* angular stability, *ML* metallic layer, *CF* center frequency of each frequency band.

offers a slightly lower profile at both frequency bands ($0.019 \lambda_0$ in the lower band and $0.039 \lambda_0$ in the higher band) compared to that of the proposed converter. However, the insertion loss at both bands (2.91 dB and 2.96 dB) was higher than that of the proposed design. Additionally, the AR bandwidths at both frequency bands in³⁷ (22.5% and 11.8%) were narrower than those of the proposed design. The proposed design also demonstrates better angular stability than the converter in³⁸. Overall, the proposed dual-band LTC polarisation converter demonstrated a significantly reduced profile size (except in^{34,38}), broader AR bandwidths, and improved angular stability, while maintaining a compact design with only one metallic layer. Despite having a slightly higher insertion loss than the other designs^{30,33,35,36}, the proposed converter's overall performance balance, particularly in terms of profile size and bandwidth, was superior among the compared designs^{28,30–38}.

Conclusion

This study presents a novel ultrathin LTC polarisation converter characterised by wide dual-band operation. The design incorporates two identical diagonally oriented C-shaped metallic strips with four diagonal parasitic strips on a single side of a single substrate layer. The strategic use of the parasitic strips is crucial for securing a near-uniform transmission amplitude and maintaining a phase difference of approximately 90° . By achieving a near-uniform transmission amplitude and a consistent phase difference close to 90° in both the lower and higher frequency bands, the converter achieved RHCP in the lower frequency band and LHCP in the higher frequency band. In addition, uniform transmittance was achieved in both frequency bands, thus facilitating LP to-CP conversion in the dual-frequency bands. The results indicate that a 3 dB AR bandwidth of the polariser can be achieved in a frequency range of 6.78–17.08 GHz (86.3%) and 25.09–36.40 GHz (36.8%) at normal electromagnetic wave incidence. The robust performance of the design underscores its potential for integration into advanced communication systems, where size, bandwidth, and polarisation control are critical.

Data availability

The datasets used and/or analysed during the current study available from the corresponding author on reasonable request.

Received: 20 September 2024; Accepted: 29 October 2024

Published online: 31 October 2024

References

- Lutz, E., Cygan, D., Dippold, M., Dolainsky, F. & Papke, W. The land mobile satellite communication channel-recording, statistics, and channel model. *IEEE Trans. Vehic Technol.* **40**, 375–386 (1991).
- Sowjanya, A. & Vakula, D. Compact dual bandpass filter using dual-split ring resonator for 5G upper microwave flexible use services. *J. Electromagn. Eng. Sci.* **22**, 434–439 (2022).
- Yuan, Y., Zhang, K., Wu, Q., Burokur, S. N. & Genevet, P. Reaching the efficiency limit of arbitrary polarization transformation with non-orthogonal metasurfaces. *Nat. Commun.* **15**, 6682 (2024).
- Zhang, J. et al. Polarization-independent grating coupler based on silicon-on-insulator. *Chin. Opt. Lett.* **13**, 091301 (2015).
- Nguyen, T. T., Kim, D. H., Choi, J. H. & Jung, C. W. Circularly polarized series array and MIMO application for sub-millimeter wave/terahertz band. *J. Electromagn. Eng. Sci.* **24**, 294–304 (2024).
- Park, I. Application of metasurfaces in the design of performance-enhanced low-profile antennas. *EPJ Appl. Metamater.* **5** (11), 1–12 (2018).
- Nkimbeng, C. H. S., Wang, H. & Park, I. Coplanar waveguide-fed bidirectional same-sense circularly polarized metasurface-based antenna. *J. Electromagn. Eng. Sci.* **21**, 210–217 (2021).
- Jung, H. B. & Lee, J. H. Theoretical and experimental investigation of N-Bit reconfigurable retrodirective metasurface. *J. Electromagn. Eng. Sci.* **24**, 51–56 (2024).
- Nkimbeng, C. H. S., Wang, H. & Park, I. Low-profile wideband unidirectional circularly polarized metasurface-based bowtie slot antenna. *IEEE Access.* **9**, 134743–134752 (2021).
- Nkimbeng, C. H. S., Wang, H., Byun, G., Park, Y. B. & Park, I. Non-uniform metasurface integrated circularly polarized end-fire dipole array antenna. *J. Electromagn. Eng. Sci.* **23**, 29–41 (2023).
- Nkimbeng, C. H. S., Wang, H. & Park, I. Crossed-dipole-shaped metasurface transmissive linear-to-circular polarization converter. *Global Symposium on Millimeter-Waves & Terahertz* (2024).
- Nkimbeng, C. H. S. et al. Ultra-wideband ultra-thin transmissive linear to circular polarization convertor based on crossed-dipole-shaped metasurface. *IEEE Access.* **12**, 120337–120346 (2024).
- Nkimbeng, C. H. S. & Park, I. Series-fed printed dipole array incorporated with linear to circular polarization metasurface converter. In *Global Symposium on Millimeter-Waves & Terahertz* 69–71 (2022).
- Ta, S. X. & Park, I. Compact wideband circularly polarized patch antenna array using metasurface. *IEEE Antennas Wirel. Propag. Lett.* **16**, 1932–1935 (2017).
- Zhang, W., Li, J. Y. & Xie, J. A broadband circular polarizer based on cross-shaped composite frequency selective surfaces. *IEEE Trans. Antennas Propag.* **65**, 5623–5627 (2017).
- Martinez-Lopez, L., Rodriguez-Cuevas, J., Martinez-Lopez, J. I. & Martynyuk, A. E. A multilayer circular polarizer based on bisected split-ring frequency selective surfaces. *IEEE Antennas Wirel. Propag. Lett.* **13**, 153–156 (2014).
- Momeni, H., Abadi, S. M. A. & Behdad, N. Wideband linear-to-circular polarization converters based on miniaturized-element frequency selective surfaces. *IEEE Trans. Antennas Propag.* **64**, 525–534 (2016).
- Lin, B. Q. et al. Wideband linear-to-circular polarization conversion realized by a transmissive anisotropic metasurface. *Chin. Phys. B.* **27**, 054204 (2018).
- Zhang, W., Li, J. Y. & Xie, J. A broadband linear-to-circular transmission polarizer based on right-angled frequency selective surfaces. *Int. J. Antennas Propag.* 8067574 (2017).
- Guo, Z., Cao, X., Gao, J., Yang, H. & Jidi, L. A novel composite transmission metasurface with dual functions and its application in microstrip antenna. *J. Appl. Phys.* **127**, 115103 (2020).
- Wang, H. B., Cheng, Y. J. & Chen, Z. N. Wideband and side-angle single-layered-substrate linear-to-circular polarization metasurface converter. *IEEE Trans. Antennas Propag.* **68**, 1186–1191 (2020).
- Gao, X. et al. Ultra-wideband linear-to-circular polarizer realized by bi-layer metasurfaces. *Opt. Express.* **30**, 18392–18401 (2022).
- Li, Y. et al. Achieving wideband linear-to-circular polarization conversion using ultra-thin bi-layered metasurfaces. *J. Appl. Phys.* **117**, 044501 (2015).

24. Lin, B. et al. A wide-angle and wideband circular polarizer using a bi-layer metasurface. *Prog. Electromag. Res.* **161**, 125–133 (2018).
25. Mirza, H. et al. Single layered swastika-shaped flexible linear-to-circular polarizer using textiles for S-band application. *Int. J. RF Microw. Comput. Aided Eng.* **28**, e21463 (2018).
26. Fei, P., Shen, Z., Wen, X. & Nian, F. A single-layer circular polarizer based on hybrid meander line and loop configuration. *IEEE Trans. Antennas Propag.* **63**, 4609–4614 (2015).
27. Ran, Y. Z. et al. Ultra-wideband linear-to-circular polarization converter with ellipse-shaped metasurfaces. *Opt. Commun.* **451**, 124–128 (2019).
28. Han, B. et al. Dual-band transmissive metasurface with linear to dual-circular polarization conversion simultaneously. *AIP Adv.* **10**, 125025 (2020).
29. Sofi, M. A., Saurav, K. & Koul, S. K. Frequency-selective surface-based compact single substrate layer dual-band transmission-type linear-to-circular polarization converter. *IEEE Trans. Microw. Theory Tech.* **68**, 4138–4149 (2020).
30. Zeng, Q., Ren, W., Zhao, H., Xue, Z. & Li, W. Dual-band transmission-type circular polariser based on frequency selective surfaces. *IET Microw. Antennas Propag.* **13**, 216–222 (2019).
31. Zhang, X. & Li, S. Asymmetric dual-band linear-to-circular converter by bi-layered chiral metamaterial. *Int. J. RF Microw. Comput. Aided Eng.* **29**, e21902 (2019).
32. Fahad, A. K., Nazir, R. & Ruan, C. Simple design of broadband polarizers using transmissive metasurfaces for dual band Ku/Ka band applications. *Sensors*. **22**, 9152 (2022).
33. Wang, H. B. & Cheng, Y. J. Single-layer dual-band linear-to-circular polarization converter with wide axial ratio bandwidth and different polarization modes. *IEEE Trans. Antennas Propag.* **67**, 4296–4301 (2019).
34. Fahad, A. K., Ruan, C., Nazir, R., Ul Haq, T. & He, W. Dual-band ultrathin meta-array for polarization conversion in Ku/Ka-band with broadband transmission. *IEEE Antennas Wirel. Propag. Lett.* **19**, 856–860 (2020).
35. Greco, F. & Arneri, E. Dual-frequency linear-to-circular polarization converter for Ka-band applications. *Sensors*. **22**, 2187 (2022).
36. Chen, Y., Zhai, G., Wang, S., Gao, J. & Ren, J. Dual-band single-layered linear-to-dual-circular polarization converter with high angle stability for satellite communication. *IEEE Antennas Wirel. Propag. Lett.* **22**, 2017–2021 (2023).
37. Zhang, B. et al. Dual-band transmissive linear to circular polarization converter with angular-stable and orthogonal polarizations. *Int. J. Microw. Wirel. Technol.* 1–9 (2023).
38. Dey, S. & Dey, S. Ultrathin single layer transmissive dual-band linear to circular converter for non-adjacent dual orthogonal circularly polarized antenna. *IEEE Access*. **12**, 65981–65986 (2024).

Acknowledgements

This work was supported in part by the National Research Foundation of Korea (NRF) grant funded by Korean Government Ministry of Science and ICT (MSIT) under Grant NRF-2022R1F1A1065324; in part by the Institute of Information and Communications Technology Planning and Evaluation (IITP) grant funded by Korean Government (MSIT), Development of 3D-NET Core Technology for High-Mobility Vehicular Service, under Grant 2022-0-00704-001; and in part by the Institute of Information and Communications Technology Planning and Evaluation (IITP) grant funded by Korean Government (MSIT) under Grant RS-2024-00396992.

Author contributions

C.H.S. Nkimbeng wrote the manuscript and performed the simulations. H. Wang designed and measured the fabricated prototype. D. Yoon prepared the measurement setup and measured the fabricated prototype. Y. B. Park addressed technical concerns regarding the measurement of the fabricated prototype, and supervised the study. I. Park conceived the idea, revised the manuscript, and supervised the study.

Declarations

Competing interests

The authors declare no competing interests.

Additional information

Correspondence and requests for materials should be addressed to Y.B.P. or I.P.

Reprints and permissions information is available at www.nature.com/reprints.

Publisher's note Springer Nature remains neutral with regard to jurisdictional claims in published maps and institutional affiliations.

Open Access This article is licensed under a Creative Commons Attribution-NonCommercial-NoDerivatives 4.0 International License, which permits any non-commercial use, sharing, distribution and reproduction in any medium or format, as long as you give appropriate credit to the original author(s) and the source, provide a link to the Creative Commons licence, and indicate if you modified the licensed material. You do not have permission under this licence to share adapted material derived from this article or parts of it. The images or other third party material in this article are included in the article's Creative Commons licence, unless indicated otherwise in a credit line to the material. If material is not included in the article's Creative Commons licence and your intended use is not permitted by statutory regulation or exceeds the permitted use, you will need to obtain permission directly from the copyright holder. To view a copy of this licence, visit <http://creativecommons.org/licenses/by-nc-nd/4.0/>.

© The Author(s) 2024